Nano Research

Open Access

Research Article

2D S-doped g-C_3N_4 and V_2CT_x nanocomposites for ultra-sensitive electrochemical sensing uric acid

Yilin Li[1], Jipeng Fan[1], Jiahe Peng[1] ✉, Yujie Zheng[3], Weiping Gong[2], and Jizhou Jiang[1] ✉

[1] *School of Environmental Ecology and Biological Engineering, Key Laboratory of Green Chemical Engineering Process of Ministry of Education, Engineering Research Center of Phosphorus Resources Development and Utilization of Ministry of Education, Wuhan Institute of Technology, Wuhan 430205, China*
[2] *Guangdong Provincial Key Laboratory for Electronic Functional Materials and Devices, Huizhou University, Huizhou 516007, China*
[3] *MOE Key Laboratory of Low-grade Energy Utilization Technologies and Systems, CQU-NUS Renewable Energy Materials & Devices Joint Laboratory, School of Energy & Power Engineering, Chongqing University, Chongqing 400044, China*

Cite this article: *Nano Research*, **2025**, *18*, 94907054. https://doi.org/10.26599/NR.2025.94907054

ABSTRACT: Accurate and sensitive detection of uric acid (UA) is crucial, as abnormal UA levels are often indicative of various diseases. This work introduces a straightforward electrochemical sensor utilizing a two-dimensional (2D) nanocomposite of S-doped g-C_3N_4 (SCN) and V_2CT_x MXene (SCN/V_2C), which was prepared via ball milling followed by calcination. The SCN/V_2C nanocomposite demonstrates superior conductivity and a reduced band gap relative to pure g-C_3N_4, leading to improved electrochemical performance for UA detection. Differential pulse voltammetry (DPV) measurements revealed a limit of detection (LOD) of 1 μM for UA and a linear response range spanning from 3 μM to 1 mM. Furthermore, experimental results confirmed the excellent stability of the SCN/V_2C nanocomposite. Density functional theory (DFT) calculations revealed that SCN/V_2C acts as a powerful electron donor, while UA functions as an efficient electron acceptor. The electron transfer between SCN/V_2C and UA is significantly greater than that with other common interfering biological molecules, leading to the highest adsorption energy of UA on the SCN/V_2C surface. This strong interaction accounts for the sensor's exceptional selectivity. This newly developed sensor provides a straightforward and highly sensitive approach for the electrochemical detection of trace levels of UA in real biological samples.

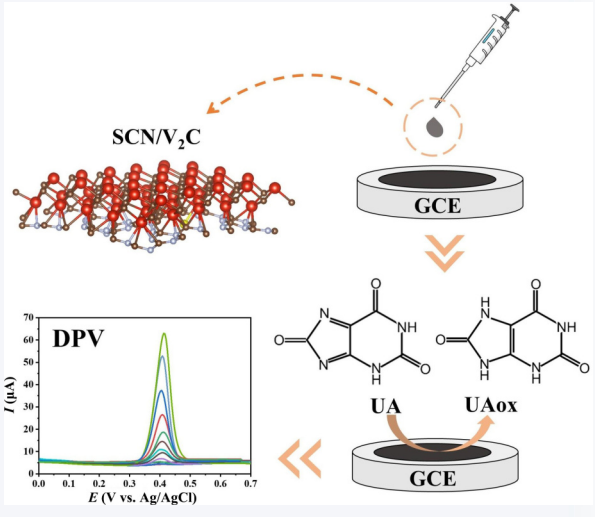

KEYWORDS: S-doped g-C_3N_4, V_2CT_x MXene, uric acid, differential pulse voltammetry, electrochemical detection

1 Introduction

Uric acid (UA) is a human metabolite, and abnormal levels in the body can lead to various diseases, including kidney injury, scurvy, and insomnia [1, 2]. Therefore, accurate and rapid detection of UA is crucial for monitoring and managing its levels, which is significant for the early diagnosis and prevention of these diseases [3–5]. Attaining a broad detection range and a low detection limit is crucial for efficient UA detection. Various established analytical techniques, including high-performance liquid chromatography (HPLC) [6], potentiometric enzyme electrode [7], colorimetry [8], spectrophotometry [9], fluorimetric technique [10], and ion chromatography [11], have been employed to measure UA levels. However, the practical application of these techniques is often limited by challenges such as high costs, cumbersome sample preparation, slow measurement times, and the need for skilled technicians [12–14]. Among the various sensing techniques available, electrochemical sensing has emerged as an attractive method for detecting biomolecules with electrochemical activity. Electrochemical sensors are increasingly preferred for UA detection because of their simplicity, rapid response, affordability, and high sensitivity [15–17].

Received: August 25, 2024; **Revised:** September 23, 2024
Accepted: September 26, 2024

✉Address correspondence to Jiahe Peng, jerry_peng.wh@foxmail.com; Jizhou Jiang, 027wit@163.com

The performance of electrochemical sensors is heavily influenced by the functional nanomaterials used on the electrodes [18]. Therefore, exploring new functional materials or composites is essential for achieving accurate and sensitive electrochemical detection of UA in various samples [19]. Recently, graphitic carbon nitride (g-C_3N_4) has gained attention in electrochemical sensor research for its distinctive layered structure, outstanding chemical stability, and superior catalytic properties [20–23]. However, the application of pure g-C_3N_4 in electrochemical sensing is limited by its low conductivity and poor electrochemical activity [24]. Elemental doping, involving the incorporation of metallic or non-metallic elements into g-C_3N_4, is a proven method to improve its properties [25–29]. Sulfur doping, in particular, has been demonstrated to alter the electronic structure of g-C_3N_4, leading to enhanced conductivity [30–32]. Another approach to enhance the electrochemical performance of g-C_3N_4 is by combining it with highly conductive materials. Since g-C_3N_4 possesses some electron migration capability, the overall electron transport efficiency of the composite can be significantly improved when combined with highly conductive materials [33]. Among these materials, MXenes—a class of 2D transition metal carbides derived from MAX phases [34–37], have been widely used in combination with g-C_3N_4 due to their high conductivity, large specific surface area, and abundant surface catalytic sites. V_2AlC, a typical vanadium based MAX phase material, has excellent mechanical properties and high temperature resistance [38–40]. V_2C, on the other hand, is the product of its etching and has a two-dimensional lamellar structure with excellent electrical conductivity, large specific surface area, and tunable surface chemistry for applications such as catalysis and energy storage [41–44]. Although several studies have investigated the synthesis and photocatalytic uses of g-C_3N_4/MXene nanocomposites [45–48], there is still limited research on the development of 2D g-C_3N_4/MXene nanocomposites for electrochemical sensing applications.

In this work, we present a straightforward approach to fabricate 2D SCN/V_2C nanocomposites for the detection of UA. The SCN/V_2C nanocomposites were synthesized through a simple process involving ball milling and calcination of sulfur powder, g-C_3N_4, and V_2C. The electrochemical performance of g-C_3N_4-based electrodes was significantly enhanced by sulfur doping and the incorporation of V_2C, owing to their high conductivity and abundant catalytic sites. The nanocomposite material was modified on the working electrode for electrochemical detection. During the process, UA will undergo oxidation reaction and generate oxidation products of UA (such as allantoin). This process usually occurs at a specific potential, and the oxidation reaction of UA is accompanied by electron transfer (Fig. 1). The current change on the electrode surface is proportional to the concentration of UA. By monitoring the current, the concentration of UA can be calculated. Utilizing the electrocatalytic properties of SCN/V_2C for UA oxidation, a differential pulse voltammetry (DPV) method was developed for UA detection. Additionally, the exceptional sensitivity and selectivity of this sensor were further analyzed using density functional theory (DFT) calculations. The adsorption energies of common biological molecules, such as UA, glucose (Glc), glutamate (Glu), and glycine (Gly), calculated through DFT, align with DPV results, confirming that the strong interaction between SCN/V_2C and UA enhance the sensor's selectivity for UA. The straightforward fabrication method used here provides important insights for designing efficient and accurate sensors capable of detecting very low concentrations of UA in real biological samples.

2 Experimental section

2.1 Preparation of V_2CT_x MXene

LiF was added to a 9 M HCl solution and stirred for half an hour to ensure complete dissolution of the salt. Subsequently, one gram of V_2AlC powder was gradually introduced into the mixture to prevent a violent exothermic reaction. The suspension was then

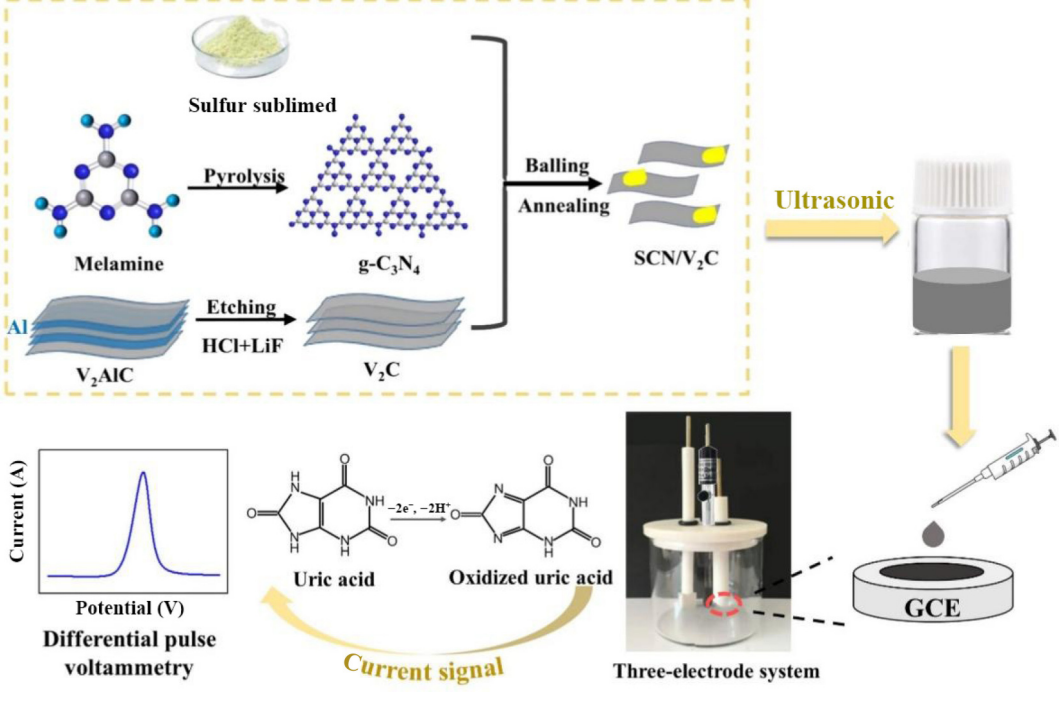

Figure 1 Schematic diagram of SCN/V_2C fabrication process and electrochemical detection of UA.

maintained at 90 °C for 24 h. After allowing the reactor to cool, the mixture was removed and washed by repeated centrifugation until the pH of the supernatant reached approximately 7. The product from the final centrifugation step was then freeze-dried.

2.2 Synthesis of g-C_3N_4

A few grams of melamine were placed in a porcelain boat and heated in a muffle furnace at a rate of 5 °C/min until reaching 550 °C. The temperature was then maintained at 550 °C for 4 h under atmospheric conditions. After cooling the porcelain boat to room temperature, the light-yellow g-C_3N_4 product was collected and ground into a powder for further use.

2.3 Fabrication of SCN/V_2C

The mixture of sulfur powder, g-C_3N_4, and V_2C was ball-milled under vacuum for 10 min. Under the condition of vacuum ball milling, the V_2C structure was relatively stable. And the electronegativity of S, C, and N elements was very close. Based on the previous Ref. [49] and our experience in preparing S-doped g-C_3N_4 materials [50, 51], S powder was easy to form SCN with g-C_3N_4 first. Then, the SCN, V_2C, and the grinding ball were mixed in a vacuum sealed cylinder. In the process of ball milling, the grinding ball with kinetic energy was given to move at high speed, so as to contact with the materials and produce force [52, 53] including impact force and shear force. The mixture produced in the first step was transferred inside to a porcelain boat. It was then heated to 550 °C at a rate of 5 °C/min in a N_2 atmosphere for 3 h. The ball-milled samples were collected and calcined at high temperatures under N_2 atmosphere to remove volatile components to purify the product [30]. At the same time, the crystal structure was improved during the process, enhancing the stability and activity of the material. The final product, named SCN/V_2C was obtained after natural cooling. The fabrication process was illustrated in Fig. 1.

2.4 Sensor fabrication

The bare 3 mm diameter glassy carbon electrode (GCE) was polished with alumina slurry on a polishing cloth, then rinsed with distilled water and ethanol. To modify the electrodes, 6 μL of the prepared dispersion was carefully applied to the surface of the pretreated GCE and dried under an infrared lamp.

2.5 Characterization

Scanning electron microscopy (SEM) was conducted with a GeminiSEM 300 field emission electron microscopy. Transmission electron microscopy (TEM) was performed using a JEM-2100 microscope. X-ray diffraction (XRD) patterns were collected with a Bruker D8 Advance TXS diffractometer, and X-ray photoelectron spectroscopy (XPS) was carried out using an ESCALAB X1+ spectrometer.

2.6 Electrochemical test

All experiments utilized a three-electrode system connected to a CHI660D electrochemical workstation (Shanghai Chenhua Instrument Co., Ltd.). The working electrode was either a bare or modified GCE, with a platinum sheet and an Ag/AgCl (3 mol/L KCl) electrode serving as the counter and reference electrodes, respectively. DPV was conducted over a potential range of 0 to 0.6 V at scan rate of 100 mV/s with a sensitivity of 0.1 mA/V, while cyclic voltammetry (CV) measurements were also carried out within this range. Electrochemical impedance spectroscopy (EIS) measurements spanned a frequency range from 1 MHz to 0.1 Hz with an amplitude of 5 mV in 0.1 mol/L KCl containing 5 mmol/L $[Fe(CN)_6]^{3-/4-}$.

2.7 Computational detail

The structural optimization and electrostatic potential (ESP) of the target molecules used in this work were performed using Gaussian09 software package [54]. Optimization of the molecular structures was performed by means of DFT with the Becke's 3 parameters and the Lee-Yang-Parr's nonlocal correlation functional (B3LYP). The basis sets for C, N, and H were 6-311 + G(d) with diffuse function for N and O atoms. The quantitative three-dimensional (3D) ESP mapping images were calculated using Multiwfn (v 3.8) [55] and plotted by VMD programs (v 1.9.3) [56].

All reported data were calculated by the density functional theory with the code of Quantum Espresso [57]. The frozen-core projector augmented-wave (PAW) method was utilized to describe the interaction between the atomic cores and the valence electron density [58]. The exchange-correlation potential was approximated within the generalized gradient approximation (GGA) using the Perdew–Burke–Ernzerhof (PBE) functional [59]. The wave function and charge density cutoff energies were optimized to 50 and 400 Ry, respectively. The Grimme-D2 term was used to observe the weak interactions [60]. The Brillouin zone in reciprocal space was sampled by a Γ-centered Monkhorst–Pack scheme with $1 \times 1 \times 1$ and $3 \times 3 \times 1$ k-point grids for geometry optimization and electronic structure calculations [61]. Bader charge analysis was used for partial charge density calculations according to interactions [62]. Maps of electron density difference were analyzed with the VESTA program [63]. The adsorption energy of adsorbates was calculated by

$$\Delta E_{*X} = E_{*X} - E_{*} - E_{X} \quad (1)$$

where E_{*X}, E_{*}, and E_X represent the energy of the total systems after adsorption, catalysts surfaces, and adsorbates, respectively.

3 Results and discussion

3.1 Morphology characterization

The morphology and surface structure of the MXene materials were examined using SEM. After etching the Al layer from the bulk V_2AlC, a lamellar structure was observed (Fig. 2(a)). Following etching, the material exhibited a multilayer MXene structure with noticeable layer separation, displaying a classic accordion-like appearance, which signifies successful synthesis [64–66]. The microstructures of the g-C_3N_4 and S-doped g-C_3N_4 (S-g-C_3N_4) samples were also analyzed by SEM. As shown in Figs. 2(b) and 2(c), both samples retained similar block-like structures, indicating that sulfur doping did not significantly alter the morphology of g-C_3N_4. After calcination, the nanocomposite material revealed both lamellar and massive structures (Fig. 2(d)), confirming the successful reaction between V_2C and S-g-C_3N_4.

The TEM images reveal that the prepared V_2CT_x is effectively exfoliated, resulting in well-defined 2D sheets (Fig. 2(e)). The g-C_3N_4 and S-g-C_3N_4 samples are composed of numerous irregular lamellar clusters that appear lumpy overall (Figs. 2(f) and 2(g)). Upon introducing V_2C, the S-g-C_3N_4 aggregates were dispersed to some extent and exhibited a more uniform growth, merging into a

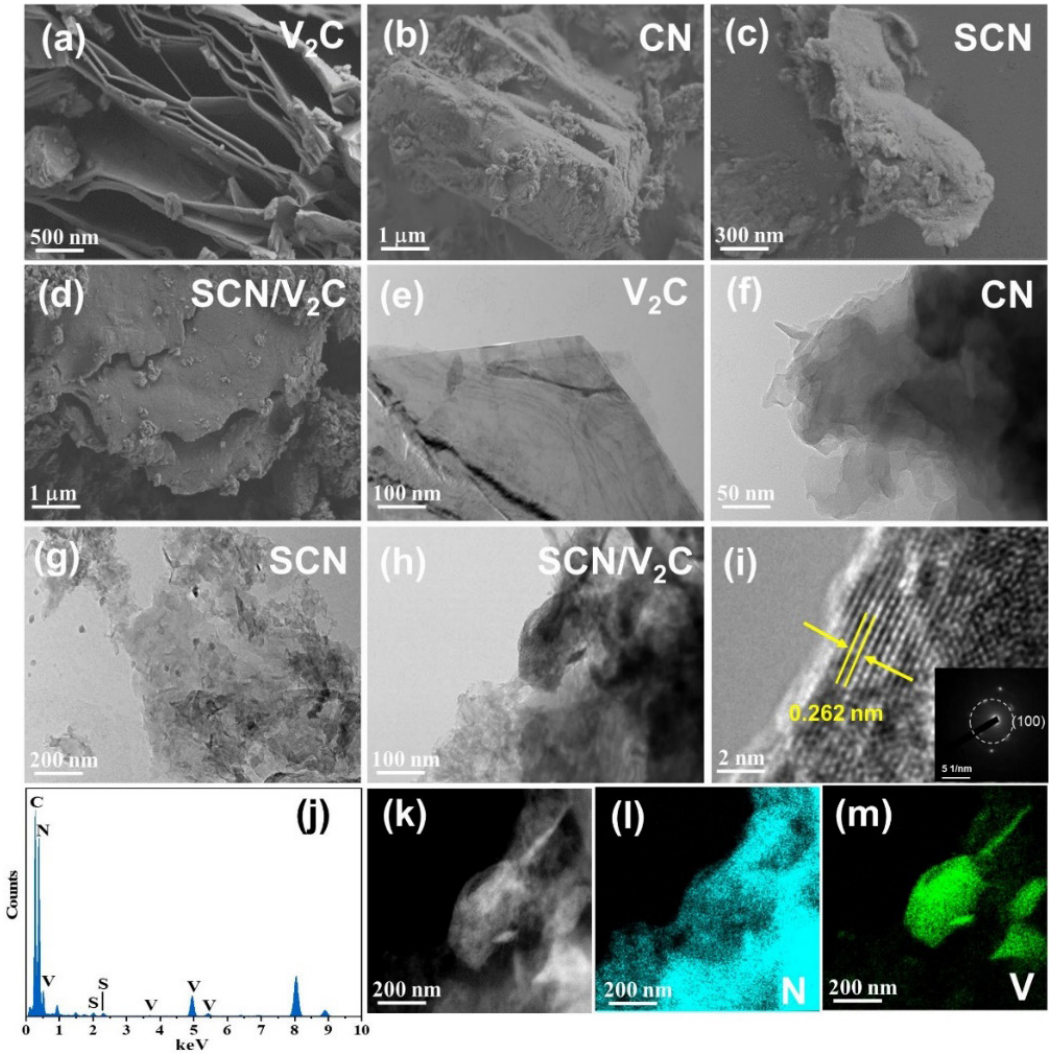

Figure 2 SEM images of (a) V_2C, (b) CN, (c) SCN, and (d) SCN/V_2C. TEM images of (e) V_2C, (f) CN, (g) SCN, and (h) SCN/V_2C. (i) HR-TEM image of SCN/V_2C (inset is the SAED pattern of V_2C). (j) TEM-EDS elemental analysis of SCN/V_2C. (k)–(m) TEM-EDS elemental mapping images of SCN/V_2C.

cohesive structure (Fig. 2(h)). As shown in Fig. 2(i), lattice fringes characteristic of V_2C MXene was observed at the edges of the nanocomposite in the high resolution TEM (HR-TEM) image. This observation not only confirms the successful synthesis of the nanocomposite material but also indicates effective contact between the two components [67]. The ordered lattice fringes verify the high crystallinity of the obtained V_2C. The lattice spacing of 0.262 nm corresponds to the (100) crystal plane [68]. The TEM-energy dispersive spectroscopy (EDS) elemental analysis of the nanocomposite material SCN/V_2C was presented in Fig. 2(j), which predominantly indicated the co-existence of C, N, S, and V elements.

TEM-EDS elemental mappings (Figs. 2(k)–2(m)) displayed a homogeneous distribution of N and V elements, suggesting that SCN and V_2C are fully mixed during the synthesis, resulting in a uniform nanocomposite material. This homogeneous distribution indicates that the synthesis process was effective, ensuring that all reactants participated evenly in the reaction and minimizing the risk of incomplete reactions or by-products [69]. The uniform distribution of elements contributes to the material's structural integrity and stability, preventing defects or degradation due to localized enrichment of elements.

3.2 Chemical structure analysis

The full X-ray photoelectron spectroscopy (XPS) spectrum of SCN/V_2C reveals the presence of C, N, S, and V, consistent with the elemental distribution observed in the SEM mapping (Fig. 3(a)). The XPS C 1s spectrum is divided into four peaks of V–C, C–C, C–N, and N–C=N [50, 70] (Fig. 3(b)). Additionally, the N 1s spectrum includes peaks associated with N–$(C)_3$, C–N–H, and C–N=C bonds (Fig. 3(c)). For the S 2p region, three main peaks correspond to S–O and C–S bonds, respectively, further confirming the successful synthesis of SCN/V_2C [51](Fig. 3(d)). Wherein, the V 2p region of SCN/V_2C, ranging from 510 to 528 eV, is deconvoluted into four main peaks, which are assigned to V–C (512.8 eV), V^{2+} (514 and 521.0 eV), V^{3+} (516.4 eV), and V^{4+} (524.5 eV) (Fig. 3(e)) [71]. The V element has a multi-valence state, and the electronic structure has outstanding adjustability. The V^{4+} usually exhibits strong catalytic performance, which can accelerate the rate of some reactions and enhance the response speed and accuracy of the sensor. The stability of V^{2+} and V^{3+} is different under different pH conditions. The performance of the sensor is improved by optimizing the pH value to improve the selectivity to specific analytes [72].Therefore, the XPS characterization results imply the removal of the Al layer and the introduction of potential

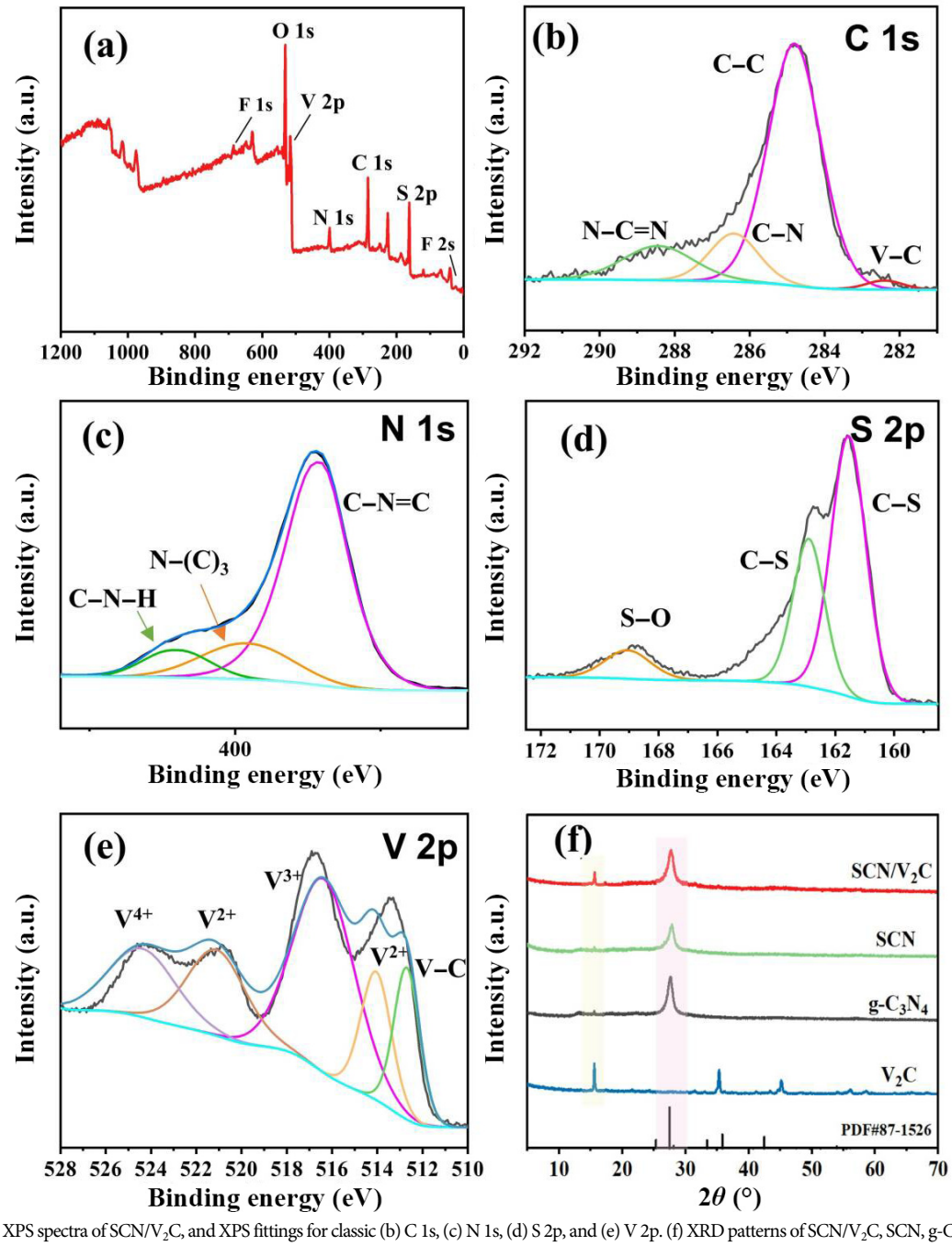

Figure 3 (a) Full XPS spectra of SCN/V_2C, and XPS fittings for classic (b) C 1s, (c) N 1s, (d) S 2p, and (e) V 2p. (f) XRD patterns of SCN/V_2C, SCN, g-C_3N_4, and V_2C.

hydrophilic functional groups, which may be due to the formation of oxygen-containing groups after etching and calcination, such as S–O [73].

Figure 3(f) shows that the diffraction peaks of SCN/V_2C are consistent with those of pure g-C_3N_4 powder. The characteristic peak at 27.5° corresponds to the (200) crystal plane of g-C_3N_4 [74, 75], corresponding in the inter-plane stacking of aromatic systems [76]. These results indicate that SCN/V_2C was successfully synthesized and the ball milling and calcination processes did not alter the crystal structure of g-C_3N_4. In summary, SCN/V_2C was successfully synthesized with its crystal structure intact.

3.3 Electrochemical behaviors

DPV can display the anodic (oxidation) current and a well-separated peak-to-peak potential difference [77]. The electron transfer abilities of the samples were evaluated using the DPV method. As shown in Fig. 4(a), the peak current of SCN/V_2C/GCE is significantly higher than that of the bare GCE and other modified electrodes, demonstrating that SCN/V_2C effectively enhances electron transfer between the electrode and the analyte. Additionally, in the presence of UA, the oxidation peak current of SCN/V_2C/GCE exceeds that of both SCN/GCE and bare GCE, underscoring the substantial improvement in electrochemical performance due to the synergistic interaction between SCN and etched V_2C compared to pure SCN or bare GCE [78].

EIS is a powerful tool for investigating the kinetics and processes at the electrode interface and was utilized to evaluate the electron transfer properties of SCN/V_2C [79, 80]. In the Nyquist diagram

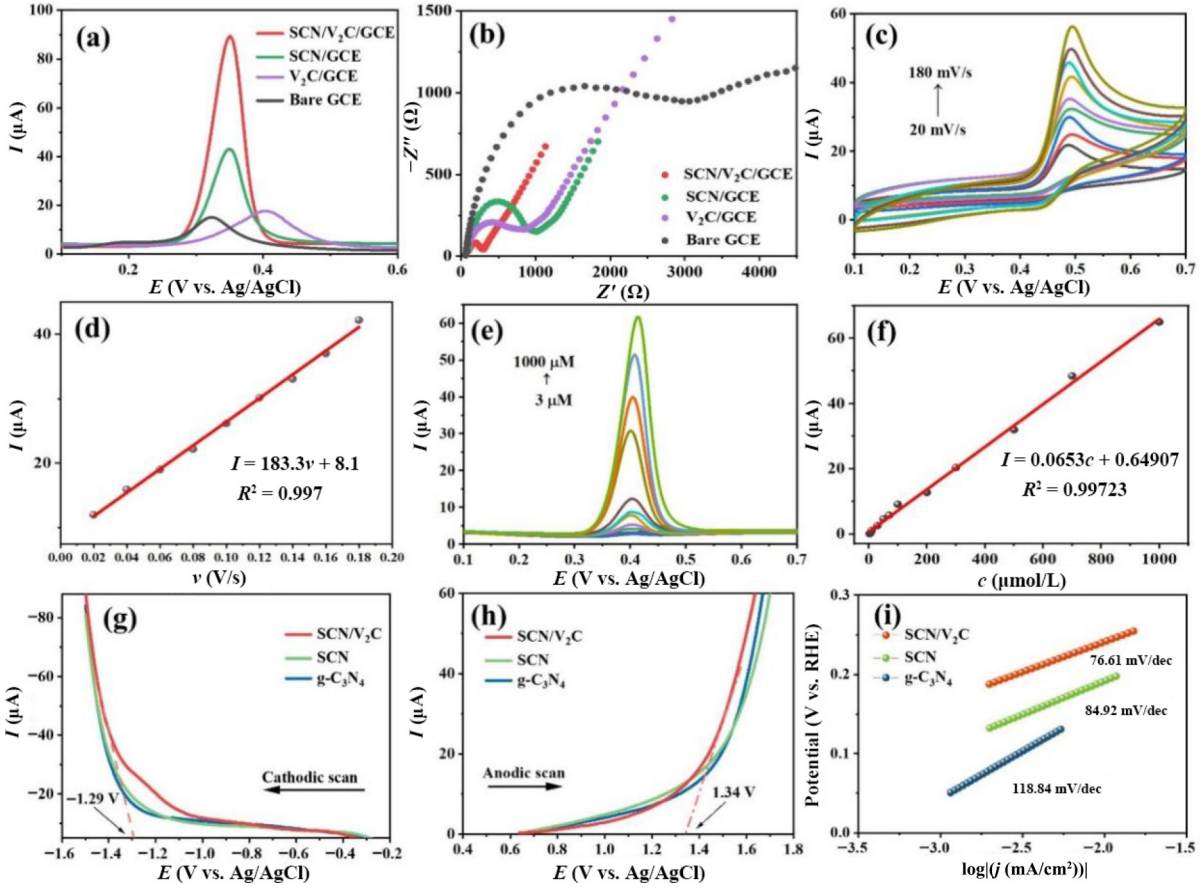

Figure 4 (a) DPV responses of the sensor to different modified electrode and (b) EIS Nyquist plots of the corresponding electrodes. (c) CV of the SCN/V_2C/GCE in 1 mM UA at various scan rates (from 20 to 180 mV/s) and (d) the plots of the redox peak currents versus scan rate. (e) DPV responses for UA (from 3 to 1000 μM) and its corresponding linear relationship between peak current and UA concentration (f). (g) Cathodic scan for determining the CBM at 5 mV/s, (h) anodic scan for determining the VBM at 5 mV/s, and (i) Tafel slope of corresponding electrodes.

(Fig. 4(b)), the semicircle diameter corresponds to the charge transfer resistance (R_{ct}) [81], with a smaller semicircle indicating a lower R_{ct}. It can be observed that when SCN/V_2C is modified onto the electrode surface, the semicircle diameter in the EIS plot decreases, signifying a lower R_{ct}. This indicates that the SCN/V_2C-modified electrode has a faster electron transfer ability and higher catalytic activity.

To elucidate the electrochemical redox mechanism of UA on SCN/V_2C/GCE, CV curves of 1 mM UA were recorded at various sweep rates. The peak current values exhibited a strong linear correlation with the sweep rate, indicating that the process occurring on the SCN/V_2C/GCE surface is adsorption-controlled. As shown in Figs. 4(c) and 4(d), the linear regression equation for UA is I_p = 183.3v + 8.1 (R^2 = 0.997), which suggests efficient electron transfer at the electrode surface [82, 83].

The DPV results for SCN/V_2C/GCE in buffer solutions with different UA concentrations are depicted in Figs. 4(e) and 4(f). The SCN/V_2C/GCE modified electrode displayed a distinct oxidation peak at around +0.4 V, with the peak current showing a consistent increase as UA concentration rose. There was a strong linear relationship between peak current and UA concentration, spanning from 3 to 1000 μM. The linear regression equation was determined to be I_p (A) = 0.0653c (mol/L) + 0.64907, with a correlation coefficient of 0.997. The limit of detection (LOD) for UA was calculated to be 1 μM. The LOD was defined by the equation LOD = 3α/b, where α is the standard deviation of the current measured on a blank sample (2.21×10^{-8} A), and b is the slope of the calibration curve (6.53×10^{-8} A/μM). The results indicate that modified GCE is a promising electrode modifier for effective electrochemical detection of UA [84].

The electronic structures of pure g-C_3N_4, S-g-C_3N_4, and SCN/V_2C nanocomposites were analyzed through their conduction band minimum (CBM) and valence band maximum (VBM) [85], as shown in Figs. 4(g) and 4(h). Measurements at a voltage of 5 mV revealed that the band gaps of pure g-C_3N_4 and SCN/V_2C nanocomposites are 2.82 and 2.63 eV, respectively. This indicates that SCN/V_2C nanocomposites possess a narrower band gap compared to pure g-C_3N_4, with values of 1.29 eV for CBM and 1.34 eV for VBM (vs. Ag/AgCl). A reduced band gap generally suggests lower electron transfer resistance at the interface, thereby improving the electron transfer efficiency of the material [86]. Narrow band gap materials typically possess more active surface sites, which improve the adsorption and activation of analytes, thereby accelerating the sensor's response speed [87]. This is supported by the experimental observation that SCN/V_2C demonstrates superior catalytic performance, as indicated by the lowest Tafel slope of 76.61 mV/dec (Fig. 4(i)). A lower Tafel slope signifies that the sensor can operate efficiently at lower potentials, which is crucial for enhancing sensor performance [88, 89].

3.4 Optimized conditions

To achieve optimal performance, we fine-tuned the electrochemical

test conditions. First, we examined how the concentration of the dispersion affected the electrochemical behavior, adjusting it while maintaining consistent coating volume and electrolyte. From the DPV results (Fig. 5(a)), the optimal dispersion concentration was found to be 2 mg/mL. Next, we investigated the impact of SCN/V_2C loading on UA detection by varying the volume of the dispersion applied while keeping the concentration at 2 mg/mL. As the loading amount increased from 4 to 6 μL, the peak current for UA significantly rose. However, further increases in loading led to a gradual decline in peak current. This decrease may be attributed to the increasing thickness of the sensing film on the GCE, which reduces the adhesion of SCN/V_2C to the electrode surface and increases the charge transfer resistance (R_{ct}). The highest UA oxidation peak was observed with a 6 μL loading amount (Fig. 5(b)). Consequently, the optimal SCN/V_2C loading was determined to be 6.0 μL.

The buffer solution type and pH are crucial in influencing the electrochemical reaction of the analyte, making their optimization vital for achieving optimal results. Figure 5(c) presents a comparison of the modified electrode's electrochemical behavior in different buffer solutions, including phosphate buffer saline (PBS), NaAc-HAc, H_3Cit-Na_3Cit, and Na_2HPO_4-H_3Cit (pH = 5.8). The findings reveal that the NaAc-HAc buffer solution provides a more favorable electrochemical response for UA. Using DPV, the effect of pH on the modified electrode's performance in a 1 mM UA solution was evaluated across a potential range of 0.1 to 0.6 V. The results indicate that the current response for UA initially increased and then decreased as pH values rose, with the peak response observed at pH 4.6. Moreover, as pH increased, the oxidation potential of UA shifted to more negative values (Fig. 5(d)), indicating the involvement of protons in the UA oxidation process [90].

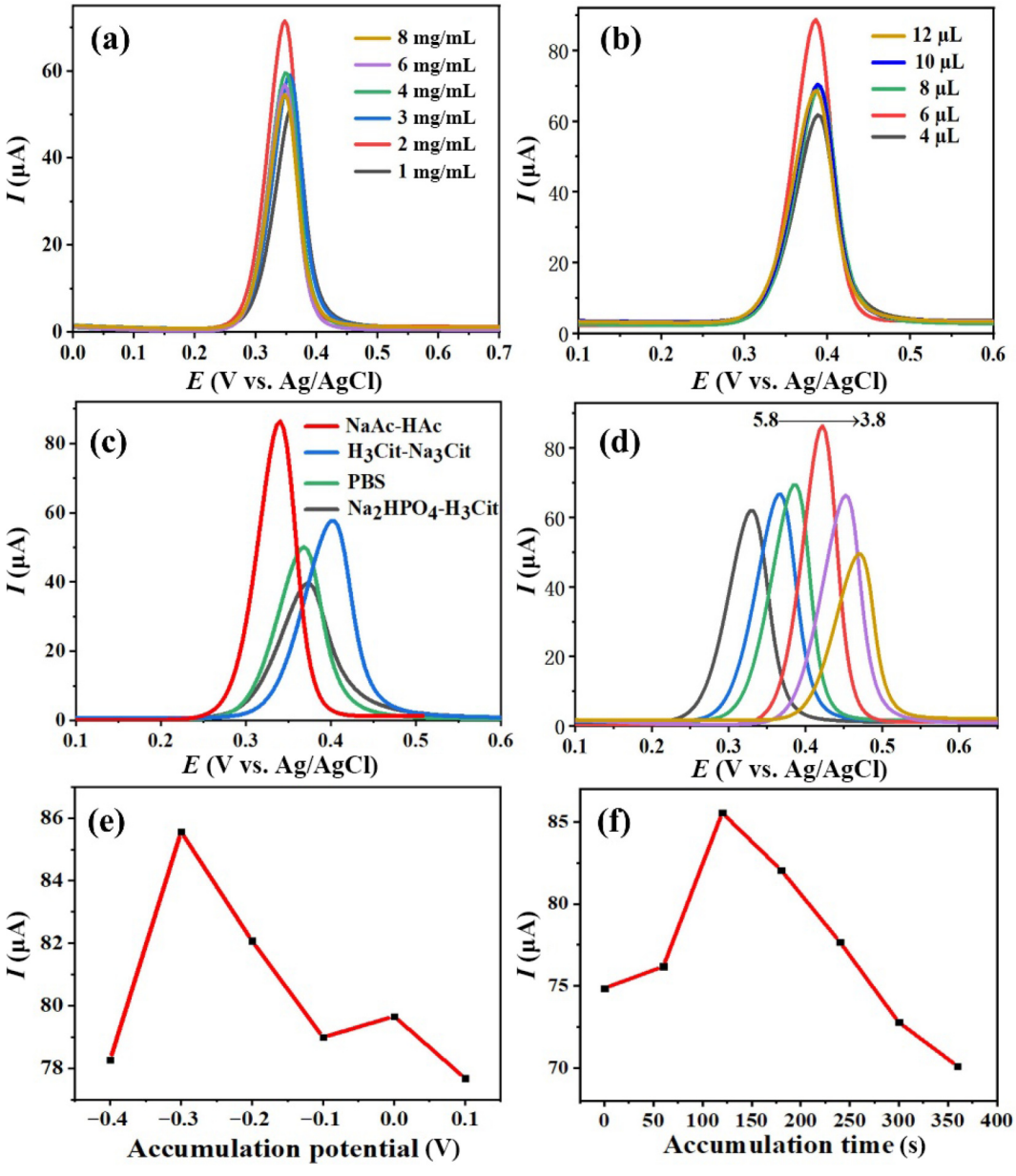

Figure 5 DPV curves of SCN/V_2C/GCE at 1 mM UA: (a) different dispersion concentrations, (b) different loading amount, (c) different types of buffer solutions, and (d) different pH values in NaAc-HAc. Plot of peak current dependence of UA on (e) accumulation potential and (f) accumulation time.

We also investigated the influence of enrichment parameters on the UA peak current. The peak current initially increased with enrichment but subsequently decreased (Figs. 5(e) and 5(f)). After thorough evaluation, the optimal enrichment conditions were determined to be an enrichment potential of –0.3 V and an enrichment time of 120 s.

3.5 Repeatability, reproducibility, stability, and anti-interference

The repeatability of the modified electrode was assessed using the DPV method in a 1 mM UA buffer solution under the optimized conditions. As shown in Fig. 6(a), the response of the same electrode maintained high accuracy with a relative standard deviation (RSD) of 8% across five repeated measurements.

Furthermore, five independent modified electrodes were prepared and used to measure the current response of 1 mM UA in parallel under the same conditions. The RSD of the current response values across these electrodes was 4% (Fig. 6(b)). These results demonstrate that the proposed sensor exhibits high repeatability and good reproducibility.

As demonstrated in Fig. 6(c), the long-term stability of the sensor was evaluated over a period of time. The sensors were vacuum-sealed and stored at 4 °C between measurements. After 10 days, the current response remained at 90% of the original value, indicating that the prepared electrodes exhibit good stability over time.

To assess the interference immunity of the modified electrode, the DPV response of UA was examined in the presence of potential interfering substances. The response of SCN/V_2C/GCE to 1 mM UA was tested alongside 100 times the concentration of common inorganic ions and 10 times the concentration of common organic small molecules [91]. As shown in Fig. 6(d), the deviation in the current responses for UA caused by these interfering substances was within ± 5%, indicating negligible effects on the oxidation current of UA. This demonstrates that SCN/V_2C/GCE exhibits excellent anti-interference properties for UA detection [92, 93].

3.6 Selectivity

Electrochemical sensors with high selectivity are designed to specifically recognize the target substance while minimizing interference from other substances, thereby enhancing the accuracy and reliability of the measurements. The selectivity of the sensor was evaluated by comparing its response to different interfering substances such as Glc, Glu, and Gly. Figure 7(a) shows the DPV responses for UA, Glc, Glu, and Gly. The results clearly indicate that the sensor produces a significant response only to the target substance, UA, while exhibiting minimal or negligible responses to the interfering substances. This demonstrates the sensor's high selectivity and its capability to distinguish UA from other compounds.

Molecular-level DFT calculations were conducted to identify the preferential adsorption sites for UA [94]. There are two surfaces present on the nanocomposite SCN/V_2C, thus two potential sites were considered: the V_2C surface (site 1) and the SCN surface (site 2). As shown in Fig. 7(b), V_2C exhibits the highest adsorption energy (–9.33 eV) for UA compared to other target molecules, indicating that UA preferentially adsorbs at site 1 [95, 96]. In addition to this, the adsorption energies of V_2C site and only etched V_2C for different target analytes were also compared. Table 1 shows that the values of adsorption energy of etched V_2C for different analytes did not differ much, while the strongest interaction between the nanocomposite V_2C site and the target UA was

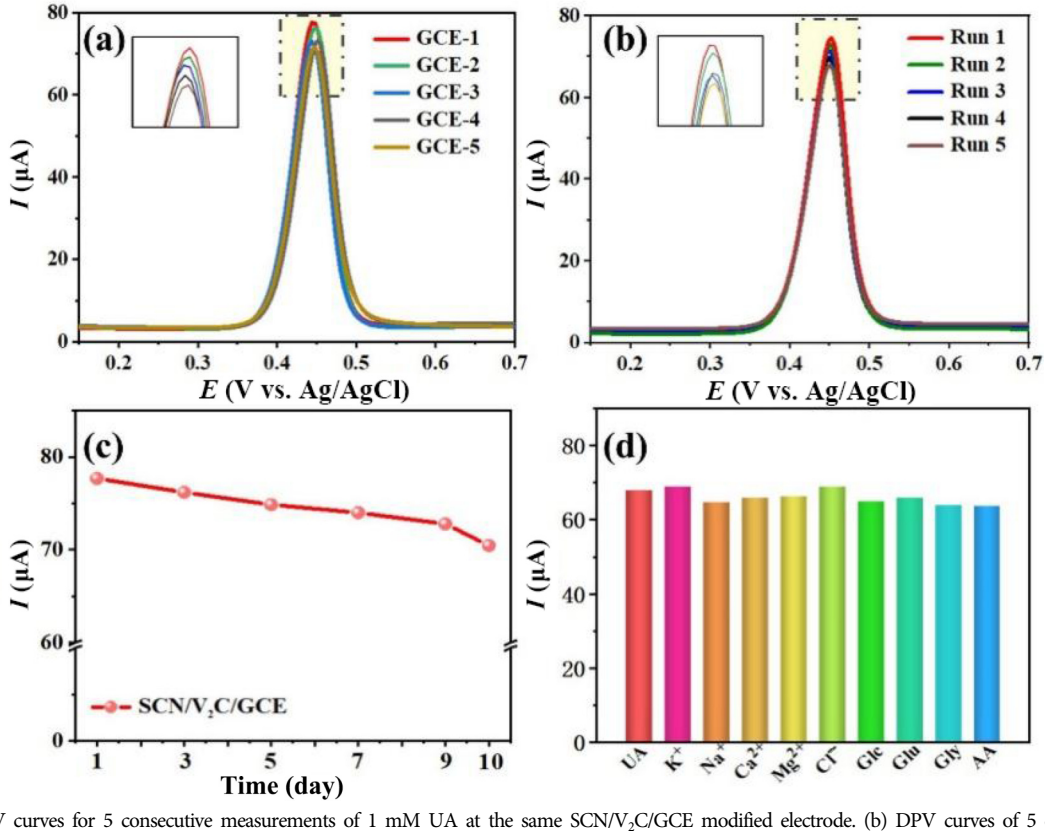

Figure 6 (a) DPV curves for 5 consecutive measurements of 1 mM UA at the same SCN/V_2C/GCE modified electrode. (b) DPV curves of 5 different modified electrodes parallel assays for 1 mM UA. (c) DPV curves for 1 mM UA over 10 days. (d) Influence of interferents on detection of 1 mM UA.

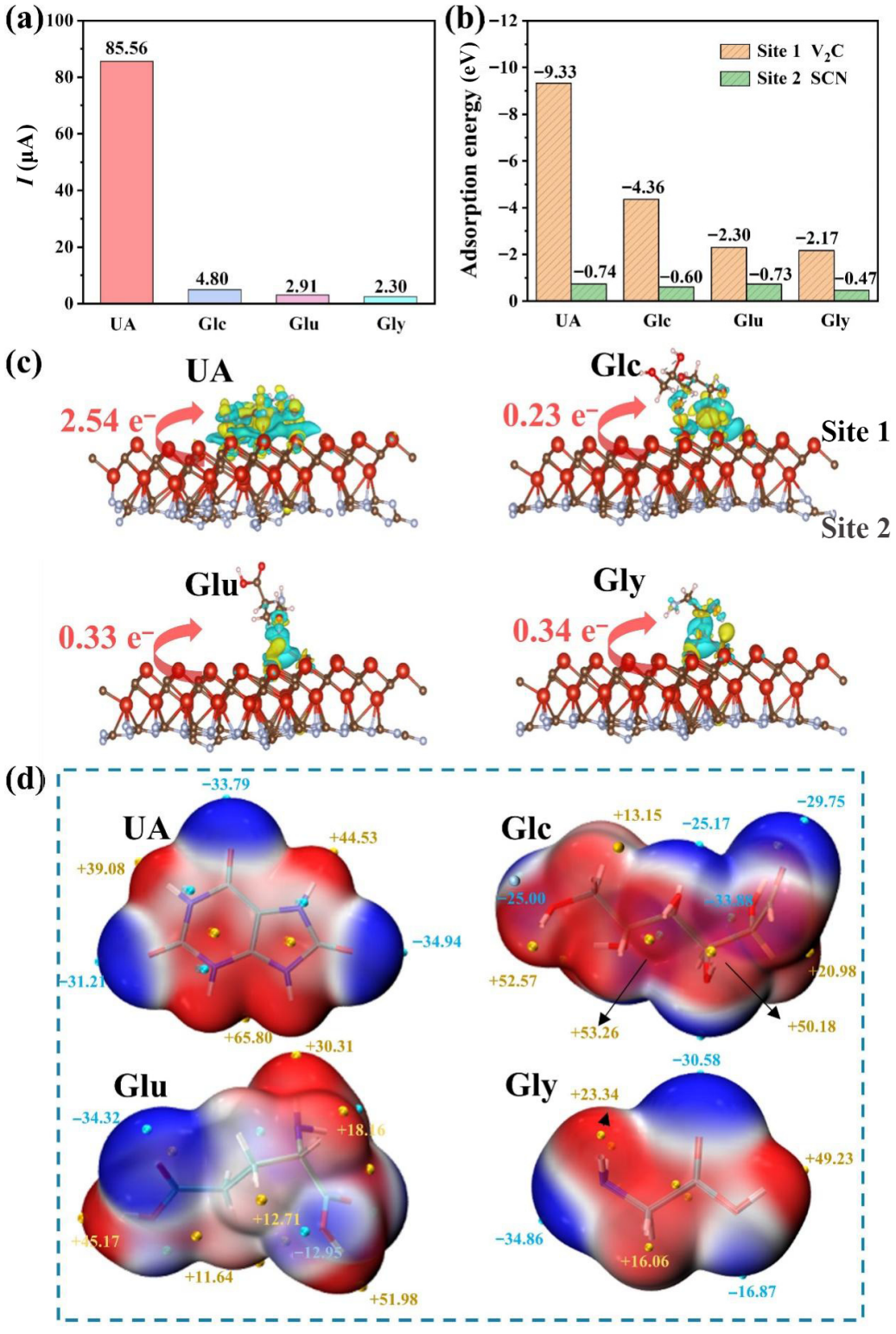

Figure 7 (a) DPV curves of SCN/V_2C/GCE with different analytes, (b) corresponding calculated adsorption energy, (c) charge density difference on the V_2C site, and (d) quantitative 3D ESP mapping images.

observed. This suggests that nanocomposite site 1 is more effective in capturing UA molecules, enhancing the current signal and improving the specificity of detection.

To further understand why site 1 has the highest adsorption energy, the charge density difference of UA on the V_2C interface was analyzed. Bader charge analysis reveals a total charge transfer of 2.54 e^- from the V_2C site to the UA, which is significantly higher than that observed for other small molecules (Fig. 7(c)). This substantial charge transfer suggests that the material exhibits high reactivity and indicates that the SCN/V_2C nanocomposite can more effectively and specifically recognize the target analyte molecule, UA [97, 98].

Table 1 The comparison of adsorption energy of V_2C site on the SCN/V_2C and V_2C after etching

Adsorption position	Adsorption energy by analytes (eV)			
	UA	Glc	Glu	Gly
V_2C site on the SCN/V_2C	−9.33	−4.36	−2.30	−2.17
V_2C after etching	−6.32	−5.01	−4.53	−3.36

ESP mapping was employed to analyze and explain the electrochemical processes occurring at the electrode interfaces [99, 100]. In electrochemical sensing, adsorption is the initial step of the reaction. The dark blue shaded areas in Fig. 7(d) represent regions with more negative charge, while the red shaded areas indicate regions with more positive charge. Analytes typically tend to adsorb in these extreme potential regions because they are more prone to charge transfer [101]. In the ESP mapping of the UA molecule, higher potential gradients, such as +65.80 and −34.94, are observed, which suggests a greater rate of electron migration. This strong interaction between UA and the nanocomposite material enhances the specific recognition of the target substance, significantly improving the selectivity and sensitivity of the electrochemical sensor.

The performance of the SCN/V_2C/GCE sensor was compared with previously reported UA sensors (Table 2). Our sensor demonstrates a lower detection limit and a wider linear range than many other sensors. Several advantages of the proposed sensor over other materials are evident. First, the integration of S-g-C_3N_4 with V_2C facilitates effective charge separation and rapid charge transport, reduces electron-hole recombination, and enhances the efficiency of the electrochemical reaction. The high specific surface area of V_2C offers more active sites, while sulfur doping introduces additional active sites and boosts the catalytic performance of the material [102]. Additionally, the sensor exhibits high sensitivity and selectivity, ensuring reliable measurements even at very low concentrations or weak signals. Finally, the SCN/V_2C nanocomposite's overall structure achieves a favorable synergy between the two components, demonstrating excellent electrochemical properties, stability, and significant potential for further development.

Table 2 Analytical comparison of linear range and LODs of other modified electrodes reported for electrochemical detection of UA

Electrode materials	Linear range (μM)	LOD (μM)	Refs.
g-C_3N_4 NS	100–1000	4.45	[103]
MoS_2 based flexible sensor	10–400	1.169	[104]
RGO–ZnO	3–330	1.08	[105]
CBNB/CNTs	1–45	0.42	[106]
Cubic Pd/rGO	4–469.5	1.6	[107]
AgNPs/rGO	10–800	8.2	[108]
Au-Cu_2O/rGO	100–900	6.5	[109]
ITO-rGO-AuNPs	10–500	10.9	[110]
MC-GO-Fe_3O_4	0.5–140	0.17	[111]
PPy/α-Fe_2O_3	5–200	1.349	[112]
Au-/RGO	8.8–53	1.8	[113]
CNCo	2–110	0.83	[114]
CeO_2	10–700	4.3	[115]
PtTi alloy	100–1000	5.3	[116]
SCN/V_2C	3–1000	1	This work

4 Conclusions

In this work, we systematically designed and successfully fabricated an SCN/V_2C/GCE sensor for the detection of UA. Through comprehensive characterization and electrochemical behavior analysis, we reached the following conclusions: (1) The introduction of new active sites through S-doping within 2D g-C_3N_4 nanosheets, combined with the high specific surface area of MXene V_2C, enhances the electrochemical reaction and significantly improves the conductivity and charge transfer efficiency of the SCN/V_2C/GCE sensor. (2) By optimizing experimental parameters, we achieved improved sensitivity and stability of the SCN/V_2C/GCE sensor, ensuring reliable performance in practical applications. (3) The SCN/V_2C/GCE sensor demonstrates high selectivity and accuracy in UA detection, maintaining a sensitive response to the target substance while effectively minimizing interference from other substances. These advancements suggest that similar processes could be applied to other nanocomposite sensors, offering new possibilities for early disease prediction and environmental detection, with substantial research value and application potential.

Data availability

Data available on request from the authors.

Acknowledgments

This work is supported by the National Natural Science Foundation of China (No. 62004143), the Key R&D Program of Hubei Province (No. 2022BAA084), and the Open Fund of the Guangdong Provincial Key Laboratory of Electronic Functional Materials and Devices (No. EFMD2024006Z).

Declaration of competing interest

The authors declare no competing financial interest.

Author contribution statement

Y. L. L., J. P. F., J. H. P., and J. Z. J. designed the proposal and wrote the manuscript. All authors have given approval to the final version of the manuscript.

Use of AI statement

None.

References

[1] Arroquia, A.; Acosta, I.; Armada, M. P. G. Self-assembled gold decorated polydopamine nanospheres as electrochemical sensor for simultaneous determination of ascorbic acid, dopamine, uric acid and tryptophan. *Mater. Sci. Eng.: C* **2020**, *109*, 110602.

[2] Wang, H.; Wang, H. T.; Yang, J. J.; Maulida, P. Y. D.; Zou, J.; Arramel, Wu, C.; Jiang, J. Z. Black phosphorus nanosheets-based effective electrochemical sensor for uric acid detection. *Carbon Lett.* **2023**, *33*, 2161–2169.

[3] Tukimin, N.; Abdullah, J.; Sulaiman, Y. Review-electrochemical detection of uric acid, dopamine and ascorbic acid. *J. Electrochem. Soc.* **2018**, *165*, B258–B267.

[4] Wang, K. D.; Wu, C.; Wang, F.; Liao, M. H.; Jiang, G. Q. Bimetallic nanoparticles decorated hollow nanoporous carbon framework as nanozyme biosensor for highly sensitive electrochemical sensing of uric acid. *Biosens. Bioelectron.* **2020**, *150*, 111869.

[5] Besbes, F.; Hsine, Z.; Mlika, R. Synthesis of heteroatoms doped reduced graphene oxide for the electrochemical determination of uric acid in commercial milk. *Carbon Lett.* **2023**, *33*, 2109–2128.

[6] Kwon, W.; Kim, J. Y.; Suh, S.; In, M. K. Simultaneous determination of creatinine and uric acid in urine by liquid chromatography-tandem mass spectrometry with polarity switching electrospray ionization. *Forensic Sci. Int.* **2012**, *221*, 57–64.

[7] Dobay, R.; G. Harsányi, Visy, C. Detection of uric acid with a new type of conducting polymer-based enzymatic sensor by bipotentiostatic technique. *Anal. Chim. Acta* **1999**, *385*, 187–194.

[8] Chen, Y. H.; Liu, A. R.; Wang, Y.; Li, P.; Zhuang, Y. R.; Sun, S. H.; Wang, D. Z.; Wei, W. A dual-mode strategy for diacetyl detection based on colorimetry and surface-enhanced Raman scattering. *Sens. Actuators B: Chem.* **2024**, *405*, 135336.

[9] Bhargava, A. K.; Lal, H.; Pundir, C. S. Discrete analysis of serum uric acid with immobilized uricase and peroxidase. *J. Biochem. Biophys. Methods* **1999**, *39*, 125–136.

[10] Fan, J.; Guo, H. Q.; Liu, G. G.; Peng, P. A. Simple and sensitive fluorimetric method for determination of environmental hormone bisphenol A based on its inhibitory effect on the redox reaction between peroxyl radical and rhodamine 6G. *Anal. Chim. Acta* **2007**, *585*, 134–138.

[11] Rocha, D. L.; Rocha, F. R. P. A flow-based procedure with solenoid micro-pumps for the spectrophotometric determination of uric acid in urine. *Microchem. J.* **2010**, *94*, 53–59.

[12] Liu, Y. Q.; Lv, J. C.; Yang, L.; Cui, Y. Electrochemical uric acid sensors: Fundamentals and commercial status. *J. Electrochem. Soc.* **2022**, *169*, 127520.

[13] Govindhan, M.; Adhikari, B. R.; Chen, A. C. Nanomaterials-based electrochemical detection of chemical contaminants. *RSC Adv.* **2014**, *4*, 63741–63760.

[14] Venkatesh, K.; Muthukutty, B.; Chen, S. M.; Karuppasamy, P.; Haidyrah, A. S.; Karuppiah, C.; Yang, C. C.; Ramaraj, S. K. Spinel $CoMn_2O_4$ nano-/micro-spheres embedded RGO nanosheets modified disposable electrode for the highly sensitive electrochemical detection of metol. *J. Ind. Eng. Chem.* **2022**, *106*, 287–296.

[15] de Almeida Ferraz, N. V.; Vasconcelos, W. S.; Silva, C. S.; Junior, S. A.; Amorim, C. G.; M. da Conceição Branco S. M. Montenegro, M.; da Cunha Areia, M. C. Gold-copper metal-organic framework nanocomposite as a glassy carbon electrode modifier for the voltammetric detection of glutathione in commercial dietary supplements. *Sens. Actuators B: Chem.* **2020**, *307*, 127636.

[16] Annalakshmi, M.; Kumaravel, S.; Chen, S. M.; Balasubramanian, P.; Balamurugan, T. S. T. A straightforward ultrasonic-assisted synthesis of zinc sulfide for supersensitive detection of carcinogenic nitrite ions in water samples. *Sens. Actuators B: Chem.* **2020**, *305*, 127387.

[17] Fu, P.; Xing, S.; Xu, M. J.; Zhao, Y.; Zhao, C. Peptide nucleic acid-based electrochemical biosensor for simultaneous detection of multiple microRNAs from cancer cells with catalytic hairpin assembly amplification. *Sens. Actuators B: Chem.* **2020**, *305*, 127545.

[18] Drummond, T. G.; Hill, M. G.; Barton, J. K. Electrochemical DNA sensors. *Nat. Biotechnol.* **2003**, *21*, 1192–1199.

[19] Zou, Y. J.; Gu, H. F.; Yang, J. J.; Zeng, T.; Yang, J.; Zhang, Y. Y. A high sensitivity strategy of nitrite detection based on CoFe@NC nanocubes modified glassy carbon electrode. *Carbon Lett.* **2023**, *33*, 2075–2086.

[20] Niu, P.; Zhang, L. L.; Liu, G.; Cheng, H. M. Graphene-like carbon nitride nanosheets for improved photocatalytic activities. *Adv. Funct. Mater.* **2012**, *22*, 4763–4770.

[21] Lu, Q. J.; Deng, J. H.; Hou, Y. X.; Wang, H. Y.; Li, H. T.; Zhang, Y. Y. One-step electrochemical synthesis of ultrathin graphitic carbon nitride nanosheets and their application to the detection of uric acid. *Chem. Commun.* **2015**, *51*, 12251–12253.

[22] Jiang, J. Z.; Ouyang, L.; Zhu, L. H.; Zheng, A. M.; Zou, J.; Yi, X. F.; Tang, H. Q. Dependence of electronic structure of g-C_3N_4 on the layer number of its nanosheets: A study by Raman spectroscopy coupled with first-principles calculations. *Carbon* **2014**, *80*, 213–221.

[23] Qin, X.; Wan, J. B.; ·Zhang, Q.; Zhang, Y. J.; Yu, H. Z.; Shi, S. W. Polyaniline-modified graphitic carbon nitride as electrode materials for high-performance supercapacitors. *Carbon Lett.* **2023**, *33*, 781–790.

[24] Ng, S. F.; Chen, X. Z.; Foo, J. J.; Xiong, M.; Ong, W. J. 2D carbon nitrides: Regulating non-metal boron-doped C_3N_5 for elucidating the mechanism of wide pH range photocatalytic hydrogen evolution reaction. *Chin. J. Catal.* **2023**, *47*, 150–160.

[25] Bhimanapati, G. R.; Lin, Z.; Meunier, V.; Jung, Y.; Cha, J.; Das, S.; Xiao, D.; Son, Y.; Strano, M. S.; Cooper, V. R. et al. Recent advances in two-dimensional materials beyond graphene. *ACS Nano* **2015**, *9*, 11509–11539.

[26] Li, J. H.; Shen, B.; Hong, Z. H.; Lin, B. Z.; Gao, B. F.; Chen, Y. L. A facile approach to synthesize novel oxygen-doped *g*-C_3N_4 with superior visible-light photoreactivity. *Chem. Commun.* **2012**, *48*, 12017–12019.

[27] Huang, Z. F.; Song, J. J.; Pan, L.; Wang, Z. M.; Zhang, X. Q.; Zou, J. J.; Mi, W. B.; Zhang, X. W.; Wang, L. Carbon nitride with simultaneous porous network and O-doping for efficient solar-energy-driven hydrogen evolution. *Nano Energy* **2015**, *12*, 646–656.

[28] Wang, D. D.; Lin, Z. X.; Miao, C.; Jiang, W.; Li, H. J.; Liu, C. B.; Che, G. B. An S-scheme photocatalyst constructed by modifying Ni-doped Sn_3O_4 micro-flowers on g-C_3N_4 nanosheets for enhanced visible-light-driven hydrogen evolution. *J. Ind. Eng. Chem.* **2022**, *113*, 380–388.

[29] Xia, X.; Xie, C.; Xu, B. G.; Ji, X. S.; Gao, G. G.; Yang, P. Role of B-doping in g-C_3N_4 nanosheets for enhanced photocatalytic NO removal and H_2 generation. *J. Ind. Eng. Chem.* **2022**, *105*, 303–312.

[30] Ma, G. X.; Ning, G. Q.; Wei, Q. S-doped carbon materials: Synthesis, properties and applications. *Carbon* **2022**, *195*, 328–340.

[31] Sun, Y. Z.; Ning, G. Q.; Qi, C. L.; Li, J. C.; Ma, X. L.; Xu, C. G.; Li, Y. F.; Zhang, X.; Gao, J. S. An advanced lithium ion battery based on a sulfur-doped porous carbon anode and a lithium iron phosphate cathode. *Electrochim. Acta* **2016**, *190*, 141–149.

[32] Ma, X. L.; Ning, G. Q.; Sun, Y. Z.; Pu, Y. J.; Gao, J. S. High capacity Li storage in sulfur and nitrogen dual-doped graphene networks. *Carbon* **2014**, *79*, 310–320.

[33] Zhu, B. C.; Zhang, L. Y.; Cheng, B.; Yu, J. G. First-principle calculation study of tri-s-triazine-based g-C_3N_4: A review. *Appl. Catal. B: Environ.* **2018**, *224*, 983–999.

[34] Naguib, M.; Mochalin, V. N.; Barsoum, M. W.; Gogotsi, Y. 25th anniversary article: MXenes: A new family of two-dimensional materials. *Adv. Mater.* **2014**, *26*, 992–1005.

[35] Jiang, J. Z.; Bai, S. S.; Zou, J.; Liu, S.; Hsu, J. P.; Li, N.; Zhu, G. Y.; Zhuang, Z. C.; Kang, Q.; Zhang, Y. Z. Improving stability of MXenes. *Nano Res.* **2022**, *15*, 6551–6567.

[36] Li, N.; Peng, J. H.; Ong, W. J.; Ma, T. T.; Arramel, Zhang, P.; Jiang, J. Z.; Yuan, X. F.; Zhang, C. F. MXenes: An emerging platform for wearable electronics and looking beyond. *Matter* **2021**, *4*, 377–407.

[37] Wang, L. N.; He, G.; Wang, W. H.; Xu, X. F.; Jiang, S. S.; Fortunato, E.; Martins, R. Energy-band engineering by 2D MXene doping for high-performance homojunction transistors and logic circuits. *J. Mater. Sci. Technol.* **2023**, *159*, 41–51.

[38] Dall'Agnese, Y.; Taberna, P. L.; Gogotsi, Y.; Simon, P. Two-dimensional vanadium carbide (MXene) as positive electrode for sodium-ion capacitors. *J. Phys. Chem. Lett.* **2015**, *6*, 2305–2309.

[39] Tan, Q. Y.; Zhuang, W.; Attia, M.; Djugum, R.; Zhang, M. X. Recent progress in additive manufacturing of bulk MAX phase components: A review. *J. Mater. Sci. Technol.* **2022**, *131*, 30–47.

[40] Yang, J. C.; Gui, Y. G.; Wang, Y. F.; He, S. S. NiO/$Ti_3C_2T_x$ MXene

nanocomposites sensor for ammonia gas detection at room temperature. *J. Ind. Eng. Chem.* **2023**, *119*, 476–484.

[41] Li, C.; Song, C. J.; Li, H.; Ye, L. Q.; Xu, Y. X.; Huang, Y. P.; Nie, G. Z.; Zhang, R. M.; Liu, W.; Huang, N. et al. Ultradurable fluorinated V_2AlC for peroxymonosulfate activation in organic pollutant degradation processes. *Chin. J. Catal.* **2022**, *43*, 1927–1936.

[42] Ganesh, P. S.; Kim, S. Y. Electrochemical sensing interfaces based on novel 2D-MXenes for monitoring environmental hazardous toxic compounds: A concise review. *J. Ind. Eng. Chem.* **2022**, *109*, 52–67.

[43] Zhou, Z. Y.; Pourhashem, S.; Wang, Z. Q.; Sun, J. W.; Ji, X. H.; Zhai, X. F.; Duan, J. Z.; Hou, B. R. Mxene structure: A key parameter in corrosion barrier performance of organic coatings. *J. Ind. Eng. Chem.* **2022**, *116*, 310–320.

[44] Luo, G. C.; Zhang, Z. L.; Wang, Y. B.; Deng, Q.; Pan, S. T.; Wang, T. F.; Li, Q. H.; Liu, K. X.; Kong, P. F.; Zhang, J. et al. A self-powered ultraviolet photodetector with van der Waals schottky junction based on TiO_2 nanorod arrays/Au-modulated V_2CT_x MXene. *J. Mater. Sci. Technol.* **2023**, *156*, 83–91.

[45] He, F.; Zhu, B. C.; Cheng, B.; Yu, J. G.; Ho, W.; Macyk, W. 2D/2D/0D $TiO_2/C_3N_4/Ti_3C_2$ MXene composite S-scheme photocatalyst with enhanced CO_2 reduction activity. *Appl. Catal. B: Environ.* **2020**, *272*, 119006.

[46] Yang, Y.; Zeng, Z. T.; Zeng, G. M.; Huang, D. L.; Xiao, R.; Zhang, C.; Zhou, C. Y.; Xiong, W. P.; Wang, W. J.; Cheng, M. et al. Ti_3C_2 Mxene/porous g-C_3N_4 interfacial schottky junction for boosting spatial charge separation in photocatalytic H_2O_2 production. *Appl. Catal. B: Environ.* **2019**, *258*, 117956.

[47] Tang, Q. J.; Sun, Z. X.; Deng, S.; Wang, H. Q.; Wu, Z. B. Decorating g-C_3N_4 with alkalinized Ti_3C_2 MXene for promoted photocatalytic CO_2 reduction performance. *J. Colloid Interface Sci.* **2020**, *564*, 406–417.

[48] Li, J. M.; Zhao, L.; Wang, S. M.; Li, J.; Wang, G. H.; Wang, J. *In situ* fabrication of 2D/3D g-C_3N_4/Ti_3C_2 (MXene) heterojunction for efficient visible-light photocatalytic hydrogen evolution. *Appl. Surf. Sci.* **2020**, *515*, 145922.

[49] Pandian, K.; Kalayarasi, J.; Gopinath, S. C. B. Metal-free sulfur-doped graphitic carbon nitride-modified GCE-based electrocatalyst for the enhanced electrochemical determination of Omeprazole in Drug formulations and Biological Samples. *Biotechnol. Appl. Biochem.* **2022**, *69*, 2766–2779.

[50] Wang, H. T.; Yu, L. L.; Peng, J. H.; Zou, J.; Gong, W. P.; Jiang, J. Z. Experimental and theoretical investigation of sulfur-doped g-C_3N_4 nanosheets/$FeCo_2O_4$ nanorods S-scheme heterojunction for photocatalytic H_2 evolution. *Nano Res.* **2024**, *17*, 8007–8016.

[51] Wang, H. T.; Yu, L. L.; Peng, J. H.; Zou, J.; Jiang, J. Z. Strategically designing and fabricating nitrogen and sulfur Co-doped g-C_3N_4 for accelerating photocatalytic H_2 evolution. *J. Mater. Sci. Technol.* **2025**, *208*, 111–119.

[52] Zhang, T. R.; Jiang, X.; Li, G. C.; Yao, Q. F.; Lee, J. Y. A red-phosphorous-assisted ball-milling synthesis of few-layered $Ti_3C_2T_x$ (MXene) nanodot composite. *ChemNanoMat* **2018**, *4*, 56–60.

[53] Zhu, K. X.; Lv, Y.; Liu, J.; Wang, W. J.; Wang, C. P.; Li, S. M.; Wang, P.; Zhang, M.; Meng, A. L.; Li, Z. J. Facile fabrication of g-C_3N_4/SnO_2 composites and ball milling treatment for enhanced photocatalytic performance. *J. Alloys Compd.* **2019**, *802*, 13–18.

[54] Frisch, M. J.; Trucks, G.; Schlegel, H. B.; Scuseria, G. E.; Robb, M. A.; Cheeseman, J. R.; Scalmani, G.; Barone, V.; Mennucci, B.; Petersson, G. A. et al. *Gaussian 09*, Revision C. 01; Gaussian Inc.: Wallingford, CT, USA, 2010.

[55] Lu, T.; Chen, F. W. Multiwfn: A multifunctional wavefunction analyzer. *J. Comput. Chem.* **2012**, *33*, 580–592.

[56] Humphrey, W.; Dalke, A.; Schulten, K. VMD: Visual molecular dynamics. *J. Mol. Graphics* **1996**, *14*, 33–38.

[57] Giannozzi, P.; Baroni, S.; Bonini, N.; Calandra, M.; Car, R.; Cavazzoni, C.; Ceresoli, D.; Chiarotti, G. L.; Cococcioni, M.; Dabo, I. et al. QUANTUM ESPRESSO: A modular and open-source software project for quantum simulations of materials. *J. Phys.: Condens. Matter* **2009**, *21*, 395502.

[58] Kresse, G.; Joubert, D. From ultrasoft pseudopotentials to the projector augmented-wave method. *Phys. Rev. B* **1999**, *59*, 1758–1775.

[59] Perdew, J. P.; Burke, K.; Ernzerhof, M. Generalized gradient approximation made simple. *Phys. Rev. Lett.* **1996**, *77*, 3865–3868.

[60] Grimme, S.; Antony, J.; Ehrlich, S.; Krieg, H. A consistent and accurate *ab initio* parametrization of density functional dispersion correction (DFT-D) for the 94 elements H-Pu. *J. Chem. Phys.* **2010**, *132*, 154104.

[61] Monkhorst, H. J.; Pack, J. D. Special points for Brillouin-zone integrations. *Phys. Rev. B* **1976**, *13*, 5188–5192.

[62] Henkelman, G.; Arnaldsson, A.; Jónsson, H. A fast and robust algorithm for Bader decomposition of charge density. *Comput. Mater. Sci.* **2006**, *36*, 354–360.

[63] Momma, K.; Izumi, F. *VESTA*: A three-dimensional visualization system for electronic and structural analysis. *J. Appl. Crystallogr.* **2008**, *41*, 653–658.

[64] Xu, J.; Hu, X. H.; Wang, X. H.; Wang, X.; Ju, Y. F.; Ge, S. H.; Lu, X. L.; Ding, J. N.; Yuan, N. Y.; Gogotsi, Y. Low-temperature pseudocapacitive energy storage in $Ti_3C_2T_x$ MXene. *Energy Storage Mater.* **2020**, *33*, 382–389.

[65] Zou, J.; Wu, J.; Wang, Y. Z.; Deng, F. X.; Jiang, J. Z.; Zhang, Y. Z.; Liu, S.; Li, N.; Zhang, H.; Yu, J. G. et al. Additive-mediated intercalation and surface modification of MXenes. *Chem. Soc. Rev.* **2022**, *51*, 2972–2990.

[66] Chu, T. S.; Wang, G. Y.; Zhang, X. Y.; Jia, Y. Y.; Dai, S.; Liu, X. Z.; Zhang, L.; Yang, X.; Zhang, B. W.; Xuan, F. Z. High-density dual-structure single-atom Pt electrocatalyst for efficient hydrogen evolution and multimodal sensing. *Nano Lett.* **2024**, *24*, 9666–9674.

[67] Wang, Z. G.; Yu, K.; Feng, Y.; Qi, R. J.; Ren, J.; Zhu, Z. Q. VO_2(p)-V_2C(MXene) grid structure as a Lithium polysulfide catalytic host for high-performance Li–S battery. *ACS Appl. Mater. Interfaces* **2019**, *11*, 44282–44292.

[68] Rong, C.; Su, T.; Li, Z. K.; Chu, T. S.; Zhu, M. L.; Yan, Y. B.; Zhang, B. W.; Xuan, F. Z. Elastic properties and tensile strength of 2D $Ti_3C_2T_x$ MXene monolayers. *Nat. Commun.* **2024**, *15*, 1566.

[69] Zhao, P.; Zhao, W. L.; Zhang, K.; Lin, H.; Zhang, X. D. Polymeric injectable fillers for cosmetology: Current status, future trends, and regulatory perspectives. *J. Appl. Polym. Sci.* **2020**, *137*, 48515.

[70] Xia, P. F.; Cheng, B.; Jiang, J. Z.; Tang, H. Localized π-conjugated structure and EPR investigation of g-C_3N_4 photocatalyst. *Appl. Surf. Sci.* **2019**, *487*, 335–342.

[71] Bai, J. B.; Zhang, Y. N.; Chen, H.; Yang, L. X.; Bai, L. J.; Wei, D. L.; Cao, X. X.; Liang, Y.; Yang, H. W. V_2CT_x MXene: A promising catalyst for low-temperature aerobic oxidative desulfurization. *Catal. Lett.* **2023**, *153*, 3103–3110.

[72] Feng, W.; Han, X. G.; Hu, H.; Chang, M. Q.; Ding, L.; Xiang, H. J.; Chen, Y.; Li, Y. H. 2D vanadium carbide MXenzyme to alleviate ROS-mediated inflammatory and neurodegenerative diseases. *Nat. Commun.* **2021**, *12*, 2203.

[73] Ren, E. H.; Cui, C.; Zhai, J. Y.; Li, A.; Tang, H.; Peng, B. Y.; Guo, R. H.; Xiao, H. Y.; Zhou, M.; Zhang, J. W. Facile synthesis of V_2CT_x@RGO composite aerogel via hydrothermal reaction and its dye adsorption performance. *J. Mater. Sci.: Mater. Electron.* **2023**, *34*, 343.

[74] Hu, C. Y.; E, L.; Hu, K. K.; Lai, L. Y.; Zhao, D.; Zhao, W.; Rong, H. Simple synthesis of 3D flower-like g-C_3N_4/TiO_2 composite microspheres for enhanced visible-light photocatalytic activity. *J. Mater. Sci.* **2020**, *55*, 151–162.

[75] Luo, X.; Dong, Y. Q.; Wang, D. Y.; Duan, Y. J.; Lei, K.; Mao, L. J.; Li, Y.; Zhao, Q.; Sun, Y. Facile synthesis of g-C_3N_4 nanosheets for effective degradation of organic pollutants via ball milling. *Rev. Adv. Mater. Sci.* **2023**, *62*, 20230123.

[76] Jin, T.; Liu, C. B.; Chen, F.; Qian, J. C.; Qiu, Y. B.; Meng, X. R.;

Chen, Z. G. Synthesis of g-C_3N_4/CQDs composite and its photocatalytic degradation property for rhodamine B. *Carbon Lett.* **2022**, *32*, 1451–1462.

[77] Shi, M. J.; Li, Y.; Wang, W. Q.; Han, R.; Luo, X. L. A super-antifouling electrochemical biosensor for protein detection in complex biofluids based on PEGylated multifunctional peptide. *ACS Sens.* **2024**, *9*, 2956–2963.

[78] Ma, L.; Zhang, Q. R.; Wu, C.; Zhang, Y.; Zeng, L. T. PtNi bimetallic nanoparticles loaded MoS_2 nanosheets: Preparation and electrochemical sensing application for the detection of dopamine and uric acid. *Anal. Chim. Acta* **2019**, *1055*, 17–25.

[79] Katz, E.; Willner, I. Probing biomolecular interactions at conductive and semiconductive surfaces by impedance spectroscopy: Routes to impedimetric immunosensors, DNA-sensors, and enzyme Biosensors. *Electroanalysis* **2003**, *15*, 913–947.

[80] Mu, X. Q.; Liu, S. L.; Zhang, M. Y.; Zhuang, Z. C.; Chen, D.; Liao, Y. R.; Zhao, H. Y.; Mu, S. C.; Wang, D. S.; Dai, Z. H. Symmetry-broken Ru nanoparticles with parasitic Ru-Co dual-single atoms overcome the volmer step of alkaline hydrogen oxidation. *Angew. Chem., Int. Ed.* **2024**, *63*, e202319618.

[81] Manikandan, R.; Kim, J.; Ishigami, A.; Cho, J. Y.; Kim, J. H.; Han, J. T.; Lee, J.; Chang, S. C. Dispersant-free supra single-walled carbon nanotubes for simultaneous and highly sensitive biomolecule sensing in *ex vivo* mouse tissues. *Carbon* **2023**, *213*, 118275.

[82] Chen, F.; Wang, J. H.; Chen, L. J.; Lin, H. L.; Han, D. X.; Bao, Y.; Wang, W.; Niu, L. A wearable electrochemical biosensor utilizing functionalized $Ti_3C_2T_x$ MXene for the real-time monitoring of uric acid metabolite. *Anal. Chem.* **2024**, *96*, 3914–3924.

[83] Ambika, A. V.; Navya, N.; Kumar, S. R. K.; Suresha, B. L. Electrochemical determination of paracetamol by SWCNT-modified carbon paste electrode: A cyclic voltammetric study. *Carbon Lett.* **2022**, *32*, 1287–1295.

[84] Amalraj, A. J. J.; Wang, S. F. Synthesis of transition metal titanium oxide ($MTiO_x$, M = Mn, Fe, Cu) and its application in furazolidone electrochemical sensor. *J. Ind. Eng. Chem.* **2022**, *111*, 356–368.

[85] Guan, Y. C.; Ren, Z. X.; Lang, Y.; Liu, T. Z.; Gong, Z.; Lv, Y. G. Preparation and photocatalytic degradation of sulfamethoxazole by g-C_3N_4 nano composite samples. *Rev. Adv. Mater. Sci.* **2023**, *62*, 20220280.

[86] Guan, D. C.; Huang, Y.; He, M. M.; Hu, G. R.; Peng, Z. D.; Cao, Y. B.; Du, K. Multilayer PEO/LLZTO composite electrolyte enables high-performance solid-state Li-ion batteries. *Ionics* **2021**, *27*, 4127–4134.

[87] Gong, Y. T.; Gu, M. M.; Yan, M. H.; Wang, G. L. Intercalated doxorubicin acting as stimulator of PbS photocathode for probing DNA-protein interactions. *Microchim. Acta* **2021**, *188*, 426.

[88] Gu, Y.; Wang, X. L.; Humayun, M.; Li, L. F.; Sun, H. C.; Xu, X. F.; Xue, X. Y.; Habibi-Yangjeh, A.; Temst, K.; Wang, C. D. Spin regulation on (Co, Ni)Se_2/C@FeOOH hollow nanocage accelerates water oxidation. *Chin. J. Catal.* **2022**, *43*, 839–850.

[89] Guo, Y. J.; Liu, Z. Y.; Zhou, D. Y.; Zhang, M. Y.; Zhang, Y.; Li, R. Z.; Liu, S. L.; Wang, D. S.; Dai, Z. H. Competition and synergistic effects of Ru-based single-atom and cluster catalysts in electrocatalytic reactions. *Sci. China Mater.* **2024**, *67*, 1706–1720.

[90] Xu, F. G.; Wang, L. W.; Wu, M. J.; Ma, G. R. Vertical growth of leaf-like Co-metal organic framework on carbon fiber cloth as integrated electrode for sensitive detection of dopamine and uric acid. *Sens. Actuators B: Chem.* **2023**, *386*, 133734.

[91] Feng, C. X.; Zhang, J. W.; Bian, C.; Li, L. Y.; Hu, R.; Chang, H. X.; Peng, F.; Peng, X. F.; Zhong, N. B. Solid-liquid-core optical fiber biosensor for highly sensitive and selective detection of 4-chlorophenol in water. *Chin. Chem. Lett.* **2023**, *34*, 108457.

[92] He, X. M.; Bai, S. S.; Jiang, J. Z.; Ong, W. J.; Peng, J. H.; Xiong, Z. G.; Liao, G. D.; Zou, J.; Li, N. Oxygen vacancy mediated step-scheme heterojunction of $WO_{2.9}$/g-C_3N_4 for efficient electrochemical sensing of 4-nitrophenol. *Chem. Eng. J. Adv.* **2021**, *8*, 100175.

[93] Qin, Z. H.; Tang, B.; Zhang, G. R.; Zhu, C. Q.; Jiang, K.; Zhang, B. W.; Xuan, F. Z. Single-atom Ni–N_4 for enhanced electrochemical sensing. *Nano Res.* **2024**, *17*, 7658–7664.

[94] Ardakani, Y. S.; Moradi, M. DFT/TDDFT study on electronic, optical and structural properties of $MAPbI_3$/$RbSnI_2Cl$ and $MAPbI_2Cl$/$RbXI_3$ (X = Pb, Sn) heterostructures. *J. Cent. South Univ.* **2023**, *30*, 1447–1460.

[95] Xiao, J. X.; Zhu, S. M.; Bu, L. J.; Zhou, S. Q. Molecularly imprinted heterostructure-based electrochemosensor for ultratrace and precise detection of 2-methylisoborneol in water. *ACS Sens.* **2024**, *9*, 524–532.

[96] Wang, L. Y.; Song, Y. H.; Luo, Y.; Wang, L. A novel covalent organic framework with multiple adsorption sites for removal of Hg^{2+} and sensitive detection of nitrofural. *J. Ind. Eng. Chem.* **2022**, *106*, 374–381.

[97] Hu, Y.; Hu, A. J.; Wang, J. W.; Niu, X. B.; Zhou, M. J.; Chen, W.; Lei, T. Y.; Huang, J. W.; Li, Y. Y.; Xue, L. X. et al. Strong intermolecular polarization to boost polysulfide conversion kinetics for high-performance lithium-sulfur batteries. *J. Mater. Chem. A* **2021**, *9*, 9771–9779.

[98] Chen, F. J.; Mu, X. Q.; Zhou, J. L.; Wang, S. C.; Liu, Z. Y.; Zhou, D. Y.; Liu, S. L.; Wang, D. S.; Dai, Z. H. Engineering the active sites of MOF-derived catalysts: From oxygen activation to activate metal-air batteries. *Chin. J. Chem.* **2024**, *42*, 2520–2535.

[99] Shukla, R.; Chopra, D. Characterization of N···O non-covalent interactions involving σ-holes: "Electrostatics" or "dispersion. *Phys. Chem. Chem. Phys.* **2016**, *18*, 29946–29954.

[100] Parcheta, M.; Świsłocka, R.; Świderski, G.; Matejczyk, M.; Lewandowski, W. Spectroscopic characterization and antioxidant properties of mandelic acid and its derivatives in a theoretical and experimental approach. *Materials* **2022**, *15*, 5413.

[101] Zou, J.; Wu, S. L.; Liu, Y.; Sun, Y. J.; Cao, Y.; Hsu, J. P.; Wee, A. T. S.; Jiang, J. Z. An ultra-sensitive electrochemical sensor based on 2D g-C_3N_4/CuO nanocomposites for dopamine detection. *Carbon* **2018**, *130*, 652–663.

[102] Jiang, J. Z.; Xiong, Z. G.; Wang, H. T.; Liao, G. D.; Bai, S. S.; Zou, J.; Wu, P. X.; Zhang, P.; Li, X. Sulfur-doped g-C_3N_4/g-C_3N_4 isotype step-scheme heterojunction for photocatalytic H_2 evolution. *J. Mater. Sci. Technol.* **2022**, *118*, 15–24.

[103] Murugan, N.; Chan-Park, M. B.; Sundramoorthy, A. K. Electrochemical detection of uric acid on exfoliated nanosheets of graphitic-like carbon nitride (g-C_3N_4) based sensor. *J. Electrochem. Soc.* **2019**, *166*, B3163–B3170.

[104] Sha, R.; Vishnu, N.; Badhulika, S. MoS_2 based ultra-low-cost, flexible, non-enzymatic and non-invasive electrochemical sensor for highly selective detection of Uric acid in human urine samples. *Sens. Actuators B: Chem.* **2019**, *279*, 53–60.

[105] Zhang, X.; Zhang, Y. C.; Ma, L. X. One-pot facile fabrication of graphene-zinc oxide composite and its enhanced sensitivity for simultaneous electrochemical detection of ascorbic acid, dopamine and uric acid. *Sens. Actuators B: Chem.* **2016**, *227*, 488–496.

[106] Baytak, A. K.; Aslanoglu, M. A novel sensitive method for the simultaneous determination of ascorbic acid, dopamine, uric acid and tryptophan using a voltammetric platform based on carbon black nanoballs. *Arabian J. Chem.* **2020**, *13*, 1702–1711.

[107] Wang, J.; Yang, B. B.; Zhong, J. T.; Yan, B.; Zhang, K.; Zhai, C. Y.; Shiraishi, Y.; Du, Y. K.; Yang, P. Dopamine and uric acid electrochemical sensor based on a glassy carbon electrode modified with cubic Pd and reduced graphene oxide nanocomposite. *J. Colloid Interface Sci.* **2017**, *497*, 172–180.

[108] Kaur, B.; Pandiyan, T.; Satpati, B.; Srivastava, R. Simultaneous and sensitive determination of ascorbic acid, dopamine, uric acid, and tryptophan with silver nanoparticles-decorated reduced graphene oxide modified electrode. *Colloids Surf. B: Biointerfaces* **2013**, *111*, 97–106.

[109] Aparna, T. K.; Sivasubramanian, R.; Dar, M. A. One-pot synthesis of

Au-Cu_2O/rGO nanocomposite based electrochemical sensor for selective and simultaneous detection of dopamine and uric acid. *J. Alloys Compd.* **2018**, *741*, 1130–1141.

[110] Mazzara, F.; Patella, B.; Aiello, G.; O'Riordan, A.; Torino, C.; Vilasi, A.; Inguanta, R. Electrochemical detection of uric acid and ascorbic acid using r-GO/NPs based sensors. *Electrochim. Acta* **2021**, *388*, 138652.

[111] Sohouli, E.; Khosrowshahi, E. M.; Radi, P.; Naghian, E.; Rahimi-Nasrabadi, M.; Ahmadi, F. Electrochemical sensor based on modified methylcellulose by graphene oxide and Fe_3O_4 nanoparticles: Application in the analysis of uric acid content in urine. *J. Electroanal. Chem.* **2020**, *877*, 114503.

[112] Wang, R. J.; Liu, S. S.; Song, X. D.; Jiang, K.; Hou, Y. H.; Cheng, Q. H.; Miao, W.; Tian, L.; Ren, Y.; Xu, S. K. Polypyrrole/α-Fe_2O_3 hybrids for enhanced electrochemical sensing performance towards uric acid. *Coatings* **2024**, *14*, 227.

[113] Wang, C. Q.; Du, J.; Wang, H. W.; Zou, C. E.; Jiang, F. X.; Yang, P.; Du, Y. K. A facile electrochemical sensor based on reduced graphene oxide and Au nanoplates modified glassy carbon electrode for simultaneous detection of ascorbic acid, dopamine and uric acid. *Sens. Actuators B: Chem.* **2014**, *204*, 302–309.

[114] Liu, L. L.; Liu, L.; Wang, Y. L.; Ye, B. C. A novel electrochemical sensor based on bimetallic metal-organic framework-derived porous carbon for detection of uric acid. *Talanta* **2019**, *199*, 478–484.

[115] Tharani, D. S.; Sivasubramanian, R. CeO_2 nanocubes-based electrochemical sensor for the selective and simultaneous determination of dopamine in the presence of uric acid and ascorbic acid. *J. Chem. Sci.* **2023**, *135*, 93.

[116] Zhao, D. Y.; Yu, G. L.; Tian, K. L.; Xu, C. X. A highly sensitive and stable electrochemical sensor for simultaneous detection towards ascorbic acid, dopamine, and uric acid based on the hierarchical nanoporous PtTi alloy. *Biosens. Bioelectron.* **2016**, *82*, 119–126.